Coherent Fourier scatterometry
a holistic tool for inspection of isolated particles or defects on gratings

Paul, Anubhav; Kolenov, Dmytro; Scholte, Thomas; Pereira, Silvania F.

DOI
10.1364/AO.503350

Publication date
2023

Document Version
Final published version

Published in
Applied Optics

Research Article Vol. 62, No. 29 / 10 October 2023 / Applied Optics 7589

applied optics

Coherent Fourier scatterometry: a holistic tool for inspection of isolated particles or defects on gratings

Anubhav Paul,* Dmytro Kolenov, Thomas Scholte, and Silvania F. Pereira

Imaging Physics Department, Faculty of Applied Sciences, Delft University of Technology, Lorentzweg 1, 2628 CJ Delft, The Netherlands
**A.Paul-1@tudelft.nl*

Received 14 August 2023; revised 14 September 2023; accepted 14 September 2023; posted 15 September 2023; published 2 October 2023

Detecting defects on diffraction gratings is crucial for ensuring their performance and reliability. Practical detection of these defects poses challenges due to their subtle nature. We perform numerical investigations and demonstrate experimentally the capability of coherent Fourier scatterometry (CFS) to detect particles as small as 100 nm and also other irregularities that are encountered usually on diffraction gratings. Our findings indicate that CFS is a viable tool for inspection of diffraction gratings.

https://doi.org/10.1364/AO.503350

1. INTRODUCTION

Diffraction gratings play a critical role in numerous technological applications, including optical devices, integrated circuits, and microfluidic systems. This diffractive optical element is widely used in many fields, including spectroscopy [1,2], spectral beam combining [3,4], chirped pulse compression [5–7], liquid crystal displays, and photonic devices [8]. These precisely engineered structures, composed of periodically spaced grooves or ridges, enable the manipulation and control of light at the nanoscale. Even though recent advancements in nanofabrication techniques have enabled the production of high-quality diffraction gratings with precise dimensions and controlled surface properties [9], the manufacturing process can introduce nanoscale contaminants or defects that can severely impact the diffraction efficiency, resulting in significant repercussions on their performance [10,11]. However, detecting these defects poses substantial challenges due to their subtle nature. Therefore, the development of effective inspection techniques for detecting and characterizing defects on diffraction gratings is of paramount importance [12].

Numerous numerical studies have explored defects in diffraction gratings, significantly advancing our understanding of their effects. Through rigorous simulations, researchers have explored the impact of various types of defects, such as nanoscale defects, scratches, or irregularities, on the diffraction characteristics of the gratings [13–15]. These studies have revealed that even small defects can lead to significant alterations in the diffracted light patterns, affecting parameters such as diffraction efficiency, spectral response, and loss [16–18]. However, despite these valuable insights, the practical detection of these defects remains a formidable task.

The detection of defects on diffraction gratings poses challenges primarily due to their nanoscale dimensions. Defects on the diffraction grating complicate the interpretation of signals, arising from scattering interactions among the grating, the defect, and higher-order scattering. Consequently, it is crucial to develop robust and sensitive inspection techniques that can overcome these challenges and reliably identify the presence of defects on diffraction gratings. The traditional tools used for the inspection of diffraction gratings are a scanning electron microscope (SEM) [19], atomic force microscope (AFM) [20], and bright field microscopy [21–23]. SEM and AFM are the benchmark techniques for nano-scale metrology because of the very high resolution of a few nanometers. However, these techniques have low throughput and can potentially inflict permanent damage to the sample, making them invasive and primarily employed in off-line mode. While bright field microscopes are non-invasive and can be used in in-line mode, they are limited by Abbe's diffraction limit and have low spatial resolution [24]. Recently, the stochastic optical reconstruction microscopy (STORM) technique, which uses the selective labeling method of fluorophores, was implemented to image defects and nanostructures of the size of tens of nanometers [25]. The technique is promising for nanoscale contamination inspection; however, as the method involves labeling, implementing it in the industry for in-line inspection remains a challenge. Alternatively, coherent Fourier scatterometry (CFS) is an optical metrology technique based on the light scattered from the object being imaged in the far field, which is very sensitive to detect small isolated particles or small changes in parameters of nanostructures [26–28]. CFS is an optical, in-line, non-invasive technique that does not require labeling [29]. CFS has been implemented for

reconstruction of parameters of diffraction gratings, and also for the detection of isolated nanoparticles on clean surfaces.

This paper presents a comprehensive numerical study on the detection of contamination in diffraction gratings using CFS by implementing rigorous 3D electromagnetic simulations, to realize the effects of a particle on a diffraction grating on the far field signatures. Furthermore, we present experimental results demonstrating the capability of CFS to detect particles as small as 100 nm on diffraction gratings with a period of 792 nm. We also demonstrate that CFS can be used to detect extra defects such as break defects, bridge defects, indentation defects, and line collapse defects, which are commonly encountered in diffraction gratings. Our findings highlight the potential of CFS as an inspection tool for diffraction gratings.

2. METHODS

A. Theory

In this section, we introduce the diffraction theory for CFS. In Fig. 1(a), the geometrical representation of a periodic 1D grating interacting with a focused beam is illustrated. The grating is defined by the geometrical parameters: period (p), line width (w), height (h), side wall angle (swa), and bias (b). b is a parameter that is introduced to define the relative position of the grating to the optical axis of the focused beam. Although the definition of the position $b = 0$ can be arbitrary, we define it as the position when the optical axis of the focused beam bisects the w, i.e., the position $x = 0$ as indicated in Fig. 1(a). We introduce a coordinate system (x, y, z) to define the grating geometry, with x-axis being parallel to the grating vector ($\vec{g}$), y-axis being perpendicular to the grating vector, and z-axis being parallel to the optical axis of the focused beam. Using angular spectrum representation formalism, we can conceive a focused beam to be an expansion of an infinite number of plane waves of different propagation directions [30]. Let us consider one such instance of the plane wave, incident on the grating by the polar angle θ_i and azimuthal angle ϕ_i. The grating diffracts the incident beam into multiple different directions as zeroth order, ±1st order, and higher orders. The angle of propagation for the nth diffraction order is given by grating's law

$$\sin\theta_i + \sin\theta_n = n\lambda/p, \tag{1}$$

where λ is the wavelength of the incident plane wave. The diffracted orders are collected by an objective lens (O) having numerical aperture (NA) and mapped to the back focal plane (BFP) based on the Fourier optics theory. The BFP is in the Fourier space with the coordinate system (ξ, η), where ξ and η are parallel to x and y, respectively. Now, if we consider the diffraction from the grating for all the plane waves, each θ_i and ϕ_i will be mapped to a different point in the BFP, i.e., the (ξ, η) plane. This mapping is limited by the NA of the objective lens. This results in each order being mapped as a circle of radius NA/λ, separated by a distance n/p in the BFP, where n is the diffraction order, as shown in Fig. 1(b). Now, any order is said to overlap if it follows the condition

$$\frac{n}{p} \le \frac{2\mathrm{NA}}{\lambda}. \tag{2}$$

Further, the amount of overlap between the diffracted orders in the BFP is defined by the overlap parameter (F) as [31]

$$F = \frac{\lambda}{\mathrm{NA} \times p}. \tag{3}$$

In Fig. 1(c), we have shown the effect of F, on the back focal plane of the objective lens. When $F > 2$, there is no overlap between the orders, i.e., all the higher orders are not collected by the objective lens. When $1 < F < 2$, there is an overlap between 0, ±1 orders but no overlap between ±1 orders is observed. Finally, when $F < 1$, there is overlap between even more diffracted orders.

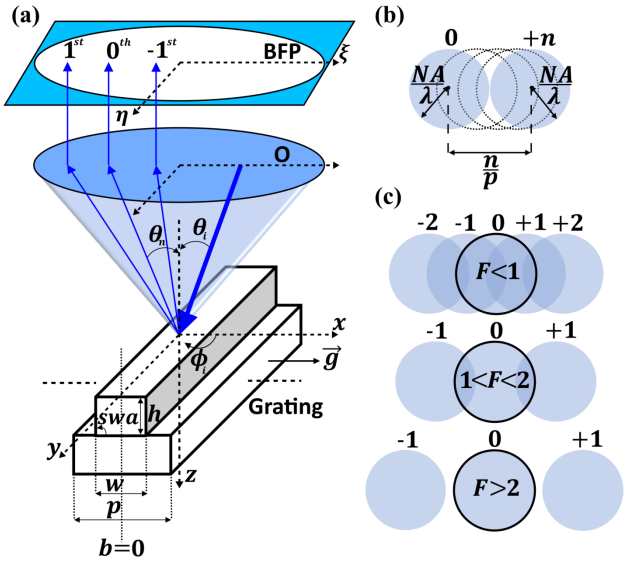

Fig. 1. (a) Schematic representation of a 1D periodic grating, having coordinate system (x, y, z), diffracting an incident beam into multiple orders. The diffracted beams are collected by an objective lens (O) having numerical aperture (NA) and propagated to the back focal plane (BFP), having coordinate system (ξ, η). (b) Condition of overlap between zeroth order and $+n$th order (having radius NA/λ), separated by distance n/p in the back focal plane. The same applies to $-n$th order. (c) Effect of overlap parameter (F), on the back focal plane of the objective lens (represented with black circles).

B. Experimental Setup

Here, we show the experimental setup of CFS. Its general configuration is shown in Fig. 2. A collimated and linearly polarized laser ($\lambda = 405$ nm) source is applied for illumination. The collimated beam from the laser passes through a non-polarizing beam splitter (BS1), which further travels to a high NA microscope objective (O) (NA = 0.9) and is focused on the Si grating sample (S). In the experiment, we do not align the polarization direction of the laser with the grating. The sample is placed on a piezo translation stage (X-Y TS), with the grating vector ($\vec{g}$) parallel to the horizontal (typically wider) scan direction (x). The translation stage can be laterally scanned in a serpentine pattern. The diffracted light from the grating is collected back by the microscope objective (O) and passes through the non-polarizing beam splitter (BS1) again. A telescopic setup consisting of two lenses (L1 and L2/L3) is added to de-magnify the Fourier plane of the objective to a split detector (SD). In this

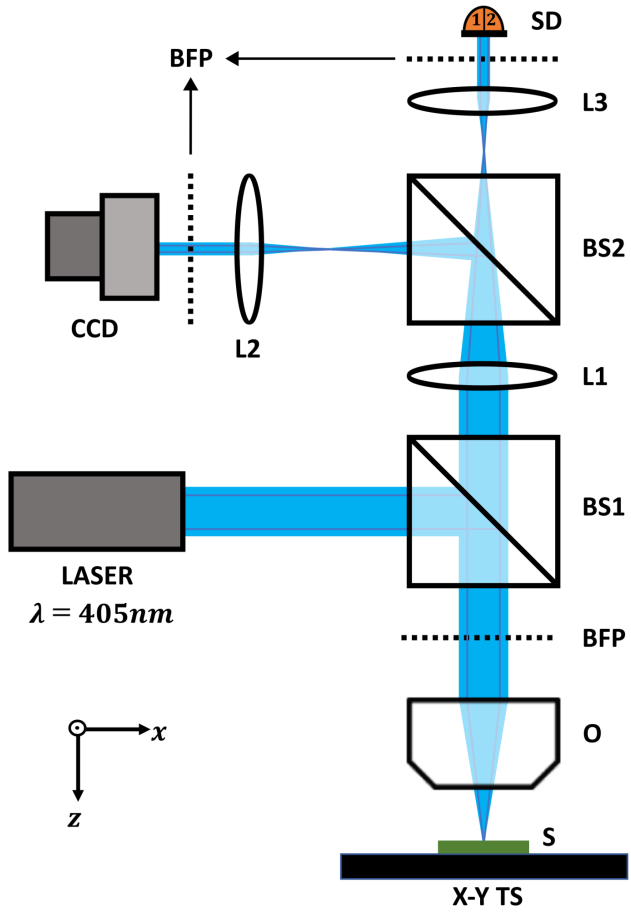

Fig. 2. Schematic of the experimental setup of coherent Fourier scatterometry (CFS).

way, the angular spectrum for all diffracted waves is detected at once for all incident plane waves within the focused spot. A charge-coupled device (CCD) camera is added in the back focal plane (BFP) of the microscope objective (O) with the help of a second non-polarizing beam splitter (BS2) to localize the region of interest in the sample.

The split detector consists of two pixels aligned perpendicular to the scan direction, and the intensity from one pixel is subtracted from the other. As a result, any specular reflections (such as the case for gratings with $F > 2$) and noise in the system are eliminated, and we observe the differential signal to be nearly zero. As the focused beam is scanned through a grating structure, i.e., bias (b) is increased from zero to period (p), for gratings with $F < 2$, the far field signature becomes asymmetric, and we observe a position-dependent differential signal. This position-dependent differential signal will repeat periodically if scanned through a large number of periods across the grating sample, i.e., the obtained differential signal is scan invariant.

C. Numerical Model

To understand the interaction of a focused beam with an isolated particle present in a grating, we need to perform accurate rigorous electromagnetic modeling. The electromagnetic problem of the interaction of a 1D grating illuminated by a focused beam has been studied using well-known rigorous coupled-wave analysis (RCWA) [31,32], which is acclaimed for applications in periodic dielectric structures. In our case, we have an aperiodic scatterer, i.e., a particle, on a periodic background, i.e., a grating. In order to treat this problem, we utilized rigorous 3D electromagnetic simulations, the finite difference time domain (3D-FDTD) method, using a commercial software package (Lumerical FDTD) [33]. In FDTD simulations, Maxwell's equations are solved in discretized Yee grids (i.e., spatial and temporal grids) in the time domain.

To mimic the experimental conditions, we model multiple periods (nine periods for this case) of the grating with and without the isolated particle at different positions [i.e., the particle is present on top of the groove (line), and the particle is present on top of the substrate of the grating], as the simulation object. We determine the number of periods of the grating in the simulation object such that the width of the focused beam (FWHM $\sim$ 302 nm) is smaller than the dimension of the simulation object ($\sim$7.128 μm). We implement perfectly matched layer (PML) boundary conditions to all the boundaries. The illumination scheme is defined as that of a TE polarized (i.e., the polarization direction at the pupil is parallel to the grating lines) plane wave of wavelength $\lambda = 405$ nm being focused by a high NA($= 0.9$) microscope objective onto the simulation object [34]. The diffracted near field from the sample is computed and sampled at the monitor plane and propagated to the far field in the FDTD simulation using Lumerical FDTD's inbuilt near-to-far field transformation (NFFT), where the computed near field is decomposed into spherical waves emanating from the sampled grids (point sources) of the monitor plane. By using Green's theorem, the radiating spherical waves at a specific distance from the monitor plane can be integrated to produce the far field signatures [35].

In Figs. 3(a)–3(c), the $y = 0$ plane, while in Figs. 3(d)–3(f), the $z = 0$ plane of the full 3D-FDTD model is shown (for bias position, $b = 0$). The simulation object's geometry is defined by the parameters, period (p), line width (w), height (h), side wall angle (swa), bias (b), and particle dimension (a). The grating and particle materials are Si ($n = 5.4254 + 0.3309i$) and Pt ($n = 1.7317 + 2.8713i$), respectively. To simulate scanning effects, we change b and we shift the simulation object along x-axis keeping the position of the source injection plane, monitor plane, and computational domain constant.

D. Sample Preparation/Deposition Method

A grating sample with geometrical parameters as detailed in Table 1 served as the substrate for particle deposition and subsequent measurements. Particle deposition is performed via electron beam induced deposition (EBID) with FEI FIB/SEM Helios G4 CX. Nominal sizes are 100 × 100 × 100 nm tungsten (W) and platinum (Pt) particles deposited on a period 792 nm diffraction grating. The same settings were used: 5 kV acceleration voltage, 1.3 pA beam current, 200 ns dwell time, −90% overlap, 0.05 μm^3/nC volume per dose. For the W material, the transverse size of the resulting particles according to the SEM image is $\approx$ 130 nm and for Pt particles $\approx$ 115 nm. The SEM measurements of the tilted plane grating with the particles deposited were not conclusive, and it is not possible to report the height of the final structures. It is our observation

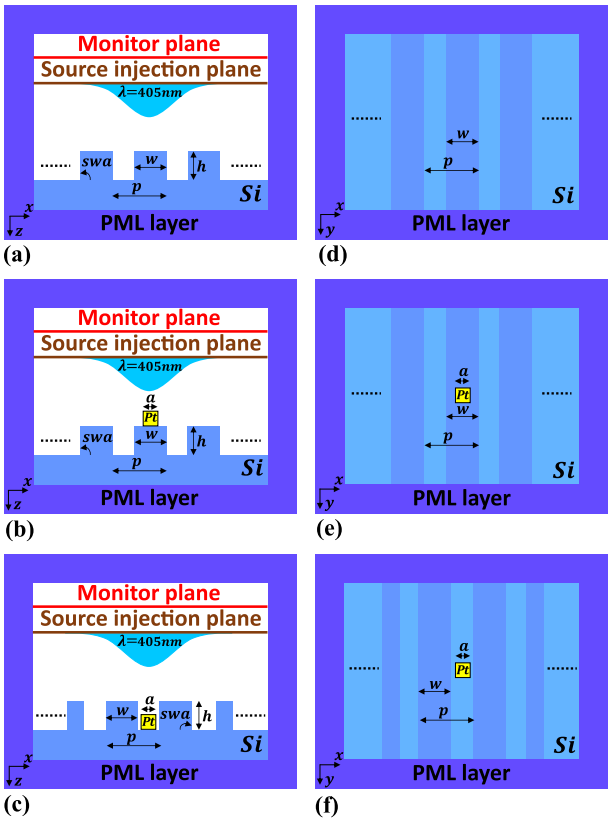

Fig. 3. 3D-FDTD simulation scheme of a grating with and without an isolated particle at different positions (shown for bias position $b = 0$). (a)–(c) Corresponding $y = 0$ plane. (d)–(f) Corresponding $z = 0$ plane.

Table 1. Geometrical Parameters of the Diffraction Grating

Grating Parameters	Nominal Values
Period (p)	792 nm
Line width (w)	396 nm
Height (h)	150 nm
Side wall angle (swa)	90°

for the deposition of similar particles directly on silicon wafers that the height of the resulting structures is less than the nominal structure. Also, the nominal size particles we deposited are lacking definition, effectively being not a cube but rather bumps of material.

3. RESULTS

A. Particle in a Periodic Grating: Numerical Study

In this section, we perform a numerical study on the influence of an isolated particle on the far field signatures of the diffraction grating. The primary objective of this numerical study is to provide a valuable tool for enhancing our understanding and interpretation of experimental results. Experimental data can often be intricate and challenging to interpret directly, making these simulations particularly valuable in aiding comprehension. As discussed earlier we are modeling an infinite periodic structure (a grating) as a finite non-periodic structure. Thus, we need to verify that our simulation model is faithful. We compare our simulated far field signatures with that of a semi-analytical method (RCWA), for the case where there is no defect/particle present on the grating. In Fig. 4(a), we have shown the far field signatures of the 3D-FDTD simulations performed without the presence of a particle [as shown in Figs. 3(a) and 3(d)] corresponding to the different bias positions ($b = 0$ nm, 66 nm, 198 nm) within a single period for a Si grating with geometrical parameters as mentioned in Table 1. In Fig. 4(b), the corresponding far field signatures obtained from RCWA have been shown. As for both simulation methods the far field signatures are consistent, we establish that our model describes the phenomena satisfactorily.

Now, to simulate the scanning of the grating with and without the isolated particle, we add a platinum (Pt) particle in the shape of a cube with dimension (a) = 100 nm in the simulation object of the grating. We consider two such cases: first, when the particle is present on top of the groove (line) of the grating [as shown in Figs. 3(b) and 3(e)], and second, when the particle is present on top of the substrate of the grating [as shown in Figs. 3(c) and 3(f)]. We perform a scan by changing the bias $b(= 0$ to $p)$ across a period with a scan step of 33 nm, with the center of the particle at the position $b = 0$ for both cases. As the bias position $b = 0$ represents the axis of symmetry for which the grating is reflection symmetric, i.e., bias $-b$ is equivalent to the mirror image of bias b, consequently, the far field signatures are also mirror images. Therefore, we obtain the far field signatures for scan positions $b = -p$ to p. For all the scan positions, we calculate the split-detector differential signal of the far field signatures. Mathematically, this can be described as

$$\mathrm{SD}(b) = \sum_{n_1=1}^{N/2}\sum_{n_2=1}^{N} I_{n_1,n_2}(b) - \sum_{n_1=N/2+1}^{N}\sum_{n_2=1}^{N} I_{n_1,n_2}(b), \quad (4)$$

where I_{n_1,n_2} is the far field signatures at the (n_1, n_2)th pixel, with N^2 being the total number of pixels in the square far field plane. In Fig. 5(a), the differential signal of the scan for the first case (represented by the red curve) along with the differential signal when the particle is absent (represented by the

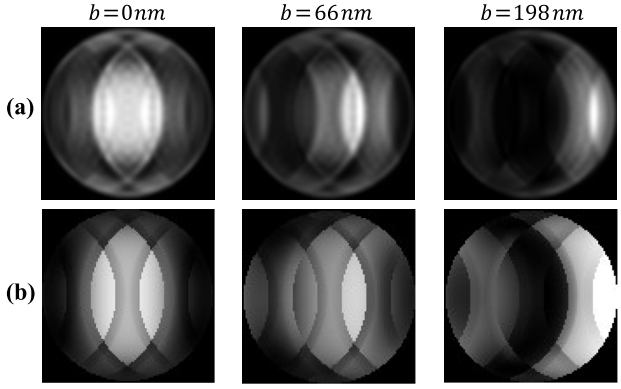

Fig. 4. Far field signatures for different bias positions ($b = 0$, 66 nm, 198 nm) of a Si grating (without particle) of period (p) = 792 nm, line width (w) = $p/2$, height (h) = 150 nm, illuminated by a TE polarized focused beam of wavelength (λ) = 405 nm. (a) Simulated using 3D-FDTD scheme; (b) simulated using RCWA.

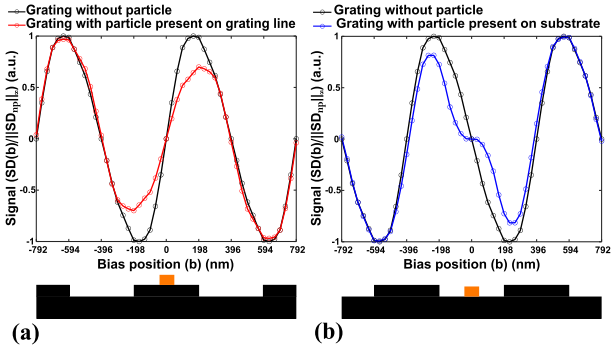

Fig. 5. Simulated differential scan signal of a *Si* grating (geometrical parameters described in Table 1) (a) with particle (dimension $a = 100$ nm) present on grating line (represented by the red curve) and without particle (represented by the black curve), with the representation of the scanned region and the position of the particle (shown in orange); (b) with particle (dimension $a = 100$ nm) present on the grating substrate (represented by the blue curve) and without particle (represented by the black curve), with the representation of the scanned region and the position of the particle (shown in orange).

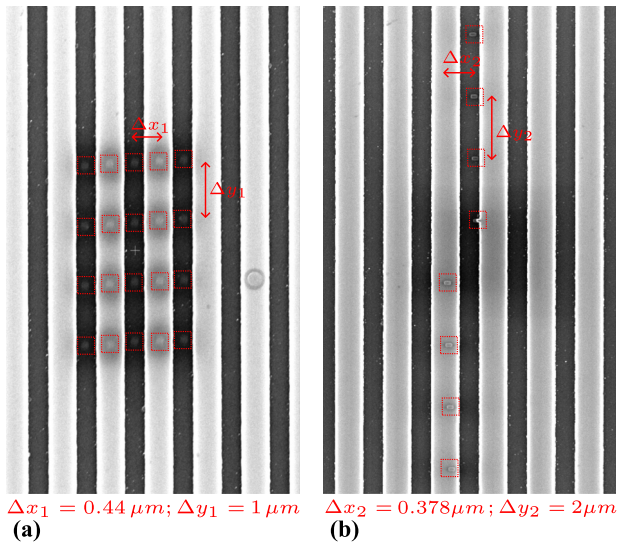

$\Delta x_1 = 0.44\,\mu m; \Delta y_1 = 1\,\mu m$
(a)

Fig. 6. SEM images of a deposition of array of (a) 4×5 tungsten (W) particles (in shape of cube $100 \times 100 \times 100$ nm); (b) 8×1 platinum (Pt) particles (in shape of cube $100 \times 100 \times 100$ nm) on a Si grating (period $p = 792$ nm, line width $w = p/2$, height $h = 150$ nm, and side wall angle $swa = 90°$) using electron beam induced deposition (EBID). The locations of the deposited particles are marked using dashed cubes for better visualization.

black curve) is plotted. Consequently in Fig. 5(b), the differential signal of the scan for the second case (represented by the blue curve) along with the differential signal when the particle is absent (represented by the black curve) is plotted. The depiction of the scanned region has been shown below in both plots of Fig. 5. The scan signal in each case is normalized to the respective scenario in the absence of the particle, such that signal $= \mathrm{SD}(b)/||\mathrm{SD}_{np}||_\infty$. The cumulative change in the signal (c) can be calculated with $c = \sum |\mathrm{signal}_{np} - \mathrm{signal}_{wp}|$, where the indices np and wp mean the case of no particle and with particle, respectively. In the case of the modeled scenario of $swa = 90°$ when the particle is present on top of the substrate of the grating, the change is $c_{swa=90°} = 6.61$, and it drops when the *swa* parameter is varied $c_{swa=85°} = 6.52$, $c_{swa=80°} = 6.55$. For the case when the particle is present on top of the grooves (lines), the change is $c_{swa=90°} = 5.18$, and it increases when the swa parameter is varied $c_{swa=85°} = 6.00$, $c_{swa=80°} = 5.90$. The simulated results in Fig. 5 indicate that the presence of an isolated particle on the grating affects the far field signatures by reducing the differential signals near the vicinity of the particle irrespective of the position of the particle on the groove (line) or substrate. But in the absence of a particle, we measure the differential signal repeating itself as we scan through the grating. These results demonstrate that this technique can detect isolated particles present on a grating.

B. Particle in a Periodic Grating: Experimental Study

In this section, we demonstrate the experimental measurements using CFS to detect particles present on a diffraction grating structure. For that, we have deposited an array of 4×5 tungsten (W) particles (in the shape of a cube $100 \times 100 \times 100$ nm) and an array of 8×1 platinum (Pt) particles (in the shape of a cube $100 \times 100 \times 100$ nm) on a Si grating (period $p = 792$ nm, line width $w = p/2$, height $h = 150$ nm, and side wall angle $swa = 90°$) using electron beam induced deposition (EBID). In Fig. 6, we show the SEM images of the grating where the particles are deposited.

The experimental setup of CFS as depicted in Fig. 2 has been used for data collection. Here, we illuminate the grating sample using a linearly polarized focused spot using a high NA $= 0.9$ microscope objective, with the polarization in an arbitrary orientation. The grating sample is placed on the piezo translation stage with the grating vector ($\vec{g}$) being parallel to scan direction (x). The diffracted field is captured by the split-detector, and the position-dependent differential signal is recorded. Now, the change in the signal in the vicinity of a particle is a reduction in the peak-to-peak value of the periodic differential signal as also discussed earlier. We can use this property, and by highlighting this change in the differential signal, we can improve the visualization of the detected particles. In Fig. 7(a), we have shown the CFS mapped data in the region where particles are deposited. Here, the breaks in the solid line indicate the presence of a particle, with the array of 4×5 W particles shown within dashed region 1 and the array of 8×1 Pt particles shown within dashed region 2. The shown CFS mapped data are rotated by an angle 1.8°, as the grating sample is placed on the piezo translation stage manually, and we cannot place the grating vector ($\vec{g}$) exactly parallel to the scan direction.

Now, we define the signal-to-noise ratio (SNR) as

$$\mathrm{SNR_{dB}} = 10 \log_{10} \frac{P_{\mathrm{signal}}}{P_{\mathrm{noise}}}. \tag{5}$$

Here, P_{signal} is the power of the signal, and P_{noise} is the power of the noise. Now, to calculate the SNR our task reduces to separating out the signal due to the particle only, without the periodic background signal. To tackle this problem, we Fourier transform our data to the frequency domain and filter out the frequencies due to the background structure. This can be done for periodic structures such as gratings where the frequencies of the background are located along the axes parallel to the

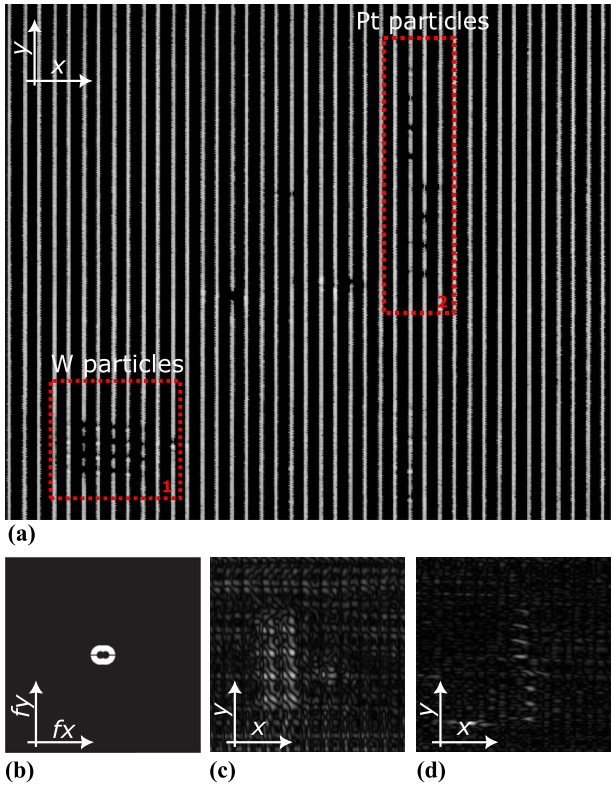

Fig. 7. (a) CFS mapped data where the W (shown within dashed region 1) and Pt (shown within dashed region 2) particles are deposited, highlighting the change in the periodic differential signal due to the particles. (b) Fourier filter used to remove the background signals. (c) CFS mapped data after filtering the background signals, where the array of W particles can be clearly seen. (d) CFS mapped data after filtering the background signals, where the array of Pt particles can be clearly seen.

direction of the grating vector ($\vec{g}$). We use a combination of rectangular and circular filters to eliminate the background frequencies due to the periodic grating as well as the noise and inverse-Fourier transform it back to the spatial domain, as shown in Fig. 7(b). From this, a significant contrast between the scattering of the structure and the scattering of the particle is achieved, making the problem analogous to particle detection on a plane substrate. In Figs. 7(c) and 7(d), we have shown the CFS mapped data after using the filter for an array of 4×5 W particles, and an array of 8×1 Pt particles, respectively. We can observe that the background from Fig. 7(a) is minimized, and we can distinguish the particles. The SNR is 7.24 dB.

C. Extra Defects

In this section, we demonstrate the capabilities of CFS to detect different types of defects usually encountered in diffraction gratings. Some of the most common defects in diffraction gratings are break defects, indentation defects, bridge defects, and line collapse defects [36]. We identify and locate these defects in Si gratings with periods $p = 378$ nm, 792 nm, 918 nm, having line width $w = p/2$, height $h = 150$ nm, and side wall angle $swa = 90°$. In Fig. 8(a), we have shown a break defect in Si gratings with period $p = 792$ nm using SEM and the corresponding

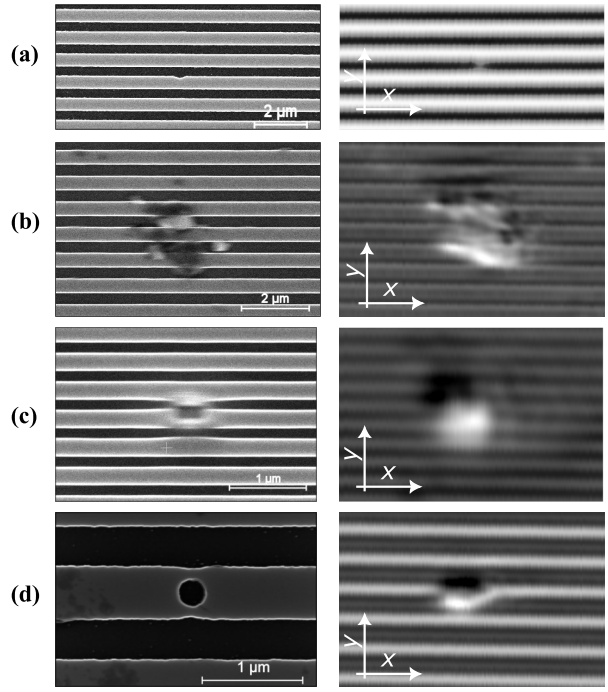

Fig. 8. SEM images (on the left) and the corresponding CFS mapped data (on the right) for various defect types in Si grating (a) break defect ($p = 792$ nm); (b) bridge defect ($p = 792$ nm); (c) line collapse defect ($p = 378$ nm); (d) indentation defect ($p = 918$ nm).

CFS mapped data. In Fig. 8(b), we have shown a bridge defect in Si gratings with period $p = 792$ nm using SEM and the corresponding CFS mapped data. In Fig. 8(c), we have shown a line collapse defect in Si gratings with period $p = 378$ nm using SEM and the corresponding CFS mapped data. In Fig. 8(d), we have shown an indentation defect in Si gratings with period $p = 918$ nm using SEM and the corresponding CFS mapped data. From the following study, we have demonstrated that CFS is a viable tool that can be used to detect different types of defects encountered in diffraction gratings.

4. CONCLUSION

In this paper, we have demonstrated the use of coherent Fourier scatterometry (CFS) as a novel tool for the inspection of diffraction gratings. We performed a numerical 3D-FDTD analysis to understand the effects of an isolated particle on the far field differential signal of a diffraction grating. The infinite periodic grating is approximated with a finite dimension of the grating; this is possible as the illuminating focused spot interacts with only a finite number of periods of the grating at any instant of time. We observed that irrespective of the position of the particle on the grating, the differential signal diminishes in the vicinity of the particle. Further, experimentally the capabilities of the tool were demonstrated by detecting tungsten W and platinum Pt particles of dimensions ~100 nm on a diffraction grating of period 792 nm. However, CFS is prone to alignment tolerances of the grating with the piezo translation stage. Further, we demonstrate that Fourier filtering can be used along with CFS to remove the background periodic signal of the grating to achieve a high SNR of 7.24 dB, although it should be noted

that the filter used is *ad hoc* and cannot be generalized just yet. Beyond the detection of particles on diffraction gratings, we demonstrated that CFS can be employed to detect different types of common defects that are encountered in diffraction gratings. These defects reduce the performance of the diffraction gratings. These results suggest that the CFS technique can be implemented for the nanoscale metrology application of periodic structures, and is a viable in-line inspection tool of semiconductor integrated circuits. Future development should include more complicated patterned structures, which will require the development of the technique to deal with edges that are arbitrarily oriented.

Funding. Nederlandse Organisatie voor Wetenschappelijk Onderzoek (Project 17-24 Synoptics No. 2).

Disclosures. The authors declare no conflicts of interest.

Data availability. Data underlying the results presented in this paper are not publicly available at this time but may be obtained from the authors upon reasonable request.

REFERENCES

1. L. Biao and Z. Y. Wen, "Design and experiment of spectrometer based on scanning micro-grating integrating with angle sensor," Infrared Phys. Technol. **62**, 29–33 (2014).
2. A. Shatokhin, A. Kolesnikov, P. Sasorov, E. Vishnyakov, and E. Ragozin, "High-resolution stigmatic spectrograph for a wavelength range of 12.5–30 nm," Opt. Express **26**, 19009–19019 (2018).
3. J. Zhang, H. Peng, X. Fu, Y. Liu, L. Qin, G. Miao, and L. Wang, "CW 50 w/M2 = 10.9 diode laser source by spectral beam combining based on a transmission grating," Opt. Express **21**, 3627–3632 (2013).
4. D. Vijayakumar, O. B. Jensen, R. Ostendorf, T. Westphalen, and B. Thestrup, "Spectral beam combining of a 980 nm tapered diode laser bar," Opt. Express **18**, 893–898 (2010).
5. D. Strickland and G. Mourou, "Compression of amplified chirped optical pulses," Opt. Commun. **56**, 219–221 (1985).
6. L. Stankevičius, T. Tamulevičius, A. Žutautas, M. Juodenas, K. Juškevicius, R. Drazdys, and S. Tamulevicius, "Diffraction efficiency optimization of multilayer dielectric mirror-based gratings for 1030 nm femtosecond lasers," Opt. Laser Technol. **126**, 106071 (2020).
7. W. Zhang, W. Kong, G. Wang, F. Xing, F. Zhang, H. Zhang, and S. Fu, "Review of pulse compression gratings for chirped pulse amplification system," Opt. Eng. **60**, 020902 (2021).
8. K. Yin, E.-L. Hsiang, J. Zou, Y. Li, Z. Yang, Q. Yang, P.-C. Lai, C.-L. Lin, and S.-T. Wu, "Advanced liquid crystal devices for augmented reality and virtual reality displays: principles and applications," Light Sci. Appl. **11**, 161 (2022).
9. Y. Wang, X. Fu, Y. Chen, L. Qin, Y. Ning, and L. Wang, "The development progress of surface structure diffraction gratings: from manufacturing technology to spectroscopic applications," Appl. Sci. **12**, 6503 (2022).
10. N. Liu, R. Dent, B. N. Hoffman, A. A. Kozlov, J. B. Oliver, A. L. Rigatti, T. J. Kessler, S. G. Demos, and A. A. Shestopalov, "Manufacturing-induced contamination in common multilayerdielectric gratings," Opt. Express **31**, 714–726 (2023).
11. L. M. Sanchez-Brea and F. J. Torcal-Milla, "Near-field diffraction of gratings with surface defects," Appl. Opt. **49**, 2190–2197 (2010).
12. J. Zhu, J. Liu, T. Xu, S. Yuan, Z. Zhang, H. Jiang, H. Gu, R. Zhou, and S. Liu, "Optical wafer defect inspection at the 10 nm technology node and beyond," Int. J. Extreme Manuf. **4**, 032001 (2022).
13. J.-I. Sugisaka, T. Yasui, and K. Hirayama, "Expansion of the difference-field boundary element method for numerical analyses of various local defects in periodic surface-relief structures," J. Opt. Soc. Am. A **32**, 751–763 (2015).
14. J.-I. Sugisaka, T. Yasui, and K. Hirayama, "Profile reconstruction of a local defect in a groove structure and the theoretical limit under the vector diffraction theory," Opt. Express **28**, 30908–30927 (2020).
15. J. Sun and C. Zheng, "Numerical scattering analysis of te plane waves by a metallic diffraction grating with local defects," J. Opt. Soc. Am. A **26**, 156–162 (2009).
16. Y. Jin, H. Guan, F. Kong, J. Wang, A. Erdmann, S. Liu, Y. Du, J. Shao, H. He, and K. Yi, "Influence of two typical defects on the near-field optical properties of multilayer dielectric compression gratings," Appl. Opt. **51**, 6683–6690 (2012).
17. C. Yang and X. Chen, "Effect of grating ruling machine system errors on grating spectral performance," Appl. Sci. **12**, 10174 (2022).
18. J. Song, N. Zhu, and S. He, "Analysis of the loss resulting from point defects for an etched diffraction grating demultiplexer by using the method of moments," J. Opt. Soc. Am. A **22**, 1620–1623 (2005).
19. A. E. Vladár and V.-D. Hodoroaba, "Characterization of nanoparticles by scanning electron microscopy," in *Characterization of Nanoparticles* (Elsevier, 2020), pp. 7–27.
20. E. Meyer, "Atomic force microscopy," Prog. Surf. Sci. **41**, 3–49 (1992).
21. O. Avci, N. L. Ünlü, A. Y. Özkumur, and M. S. Ünlü, "Interferometric reflectance imaging sensor (IRIS)—a platform technology for multiplexed diagnostics and digital detection," Sensors **15**, 17649–17665 (2015).
22. J. T. Trueb, O. Avci, D. Sevenler, J. H. Connor, and M. S. Ünlü, "Robust visualization and discrimination of nanoparticles by interferometric imaging," IEEE J. Sel. Top. Quantum Electron. **23**, 394–403 (2016).
23. J. Ortega-Arroyo and P. Kukura, "Interferometric scattering microscopy (ISCAT): new frontiers in ultrafast and ultrasensitive optical microscopy," Phys. Chem. Chem. Phys. **14**, 15625–15636 (2012).
24. E. Abbe, "Beiträge zur theorie des mikroskops und der mikroskopischen wahrnehmung," Archiv für mikroskopische Anatomie **9**, 413–468 (1873).
25. D. T. Nguyen, S. Mun, H. Park, U. Jeong, G.-H. Kim, S. Lee, C.-S. Jun, M. M. Sung, and D. Kim, "Super-resolution fluorescence imaging for semiconductor nanoscale metrology and inspection," Nano Lett. **22**, 10080–10087 (2022).
26. S. Roy, M. Bouwens, L. Wei, S. F. Pereira, H. P. Urbach, and P. Van Der Walle, "High speed low power optical detection of sub-wavelength scatterer," Rev. Sci. Instrum. **86**, 123111 (2015).
27. H.-F. Kuo, M. Faisal, and S.-F. Su, "Linewidth reconstruction employing a radial basis function network in optical scatterometry," IEEE Access **4**, 6739–6748 (2016).
28. S. Roy, A. Assafrao, S. F. Pereira, and H. P. Urbach, "Coherent Fourier scatterometry for detection of nanometer-sized particles on a planar substrate surface," Opt. Express **22**, 13250–13262 (2014).
29. D. Kolenov, I. Zadeh, R. Horsten, and S. F. Pereira, "Direct detection of polystyrene equivalent nanoparticles with a diameter of 21 nm (λ/19) using coherent Fourier scatterometry," Opt. Express **29**, 16487–16505 (2021).
30. J. J. Stamnes, *Waves in Focal Regions: Propagation, Diffraction and Focusing of Light, Sound and Water Waves* (Routledge, 2017).
31. N. Kumar, P. Petrik, G. K. Ramanandan, O. El Gawhary, S. Roy, S. F. Pereira, W. M. Coene, and H. P. Urbach, "Reconstruction of sub-wavelength features and nano-positioning of gratings using coherent Fourier scatterometry," Opt. Express **22**, 24678–24688 (2014).
32. N. Kumar, O. El Gawhary, S. Roy, S. F. Pereira, and H. P. Urbach, "Phase retrieval between overlapping orders in coherent Fourier scatterometry using scanning," J. Eur. Opt. Soc.-Rapid Publ. **8**, 13048 (2013).
33. "Ansys Lumerical FDTD solutions," https://www.lumerical.com/.
34. L. Thibon, L. E. Lorenzo, M. Piché, and Y. De Koninck, "Resolution enhancement in confocal microscopy using Bessel-Gauss beams," Opt. Express **25**, 2162–2177 (2017).
35. İ. R. Çapoğlu, J. D. Rogers, A. Taflove, and V. Backman, "The microscope in a computer: image synthesis from three-dimensional full-vector solutions of Maxwell's equations at the nanometer scale," Prog. Opt. **57**, 1–91 (2012).
36. B. Dey, D. Goswami, S. Halder, K. Khalil, P. Leray, and M. A. Bayoumi, "Deep learning-based defect classification and detection in SEM images," Proc. SPIE **PC12053**, PC120530K (2022).